Instantaneous Pressure and Material Acceleration Measurements using a Four Exposure PIV System

X. Liu, J. Katz

Abstract: A non-intrusive technique for measuring the instantaneous spatial pressure distribution over a sample area in a flow field has been developed. This technique utilizes four-exposure PIV to measure the distribution of material acceleration, and integrates it to obtain the pressure distribution. Two cameras and perpendicularly polarized Nd:Yag lasers are used for recording four exposures on separate frames. Images 1 and 3 are used for measuring the first velocity distribution, whereas images 2 and 4 provide the second velocity map. The material acceleration is calculated from the velocity difference in sample areas shifted relative to each other according to the local velocity. Exposing both cameras to the same stationary particle field and cross-correlating the images enables the precision matching of the two fields of view. Application of local image deformation correction to velocity vectors measured by the two cameras reduces the error due to relative misalignment and image distortion to about 0.01 pixels. An efficient and accurate acceleration integration algorithm has also been developed. Validation tests of the principles of the technique using synthetic images of rotating and stagnation point flows show that the standard deviation of the measured pressure from the exact value is about 1.0%. This system is used to measure the instantaneous pressure and acceleration distributions of a 2D cavity flow field and sample results are presented.

1
Introduction

Knowledge of the pressure distribution in a flow field is a primary concern in many engineering applications. The pressure is the dominant contributor to the lift and form drag for a body moving in fluid. Wall pressure fluctuations are responsible for excitation of structures, leading to flow induced vibrations and noise (Blake, 1986). In turbulence research, the velocity-pressure-gradient tensor in the Reynolds stress transport equation, which is typically decomposed into the pressure diffusion and the pressure-strain tensors, is a key unresolved parameter in modeling of turbulence (Pope, 2000; Girimaji, 2000). However, due to lack of experimental techniques for simultaneous measurements of pressure and velocity gradients simultaneously, the velocity-pressure-gradient tensor has never been measured directly. Available experimental data on pressure diffusion has been inferred experimentally in simple geometries from a balance of the other terms in the turbulence kinetic energy transport equations (Gutmark and Wygnanski 1976; Wygnanski and Fiedler 1969; Liu and Thomas 2004). The only source of reliable information is direct numerical simulation (DNS) data, which are also limited to simple geometries and low Reynolds numbers.

   Pressure is also of fundamental importance for understanding and modeling cavitation. It is well established that cavitation inception occurs when small bubbles or nuclei in liquid grow explosively due to exposure to low pressure (Brennen, 1995; Arndt, 2002). However, due to lack of the experimental capability, we have very little data on the instantaneous pressure distributions away from boundaries, e.g. in turbulent free shear layers and within tip vortices. To date the only available techniques for pressure measurement away from boundaries are based on Pitot-tube type of probes, such as five hole and seven hole probes. However, these probes are intrusive, not suitable for dynamic measurement due to a limited frequency response, and can only perform point measurements. Although limited instantaneous pressure measurements were performed in the past using microscopic bubbles as pressure sensors (Ooi and Acosta, 1983; O'Hern 1990; Ran and Katz, 1994), they were not performed simultaneously with velocity

Xiaofeng Liu, Joseph. Katz, Department of Mechanical Engineering, Johns Hopkins University, Baltimore, Maryland 21218, USA

Correspondence to:
Dr.Joseph Katz, Department of Mechanical Engineering/JHU, 223 Latrobe Hall/3400 N. Charles St., Baltimore, Maryland 21218, USA
E-mail: katz@jhu.edu

measurements, and more importantly, provided very limited data points. To date even with the detailed velocity

measurements, and more importantly, provided very limited data points. To date even with the detailed velocity measurements provided by PIV, we still do not have direct experimental data on the local instantaneous pressure causing cavitation inception in high Reynolds number flows. In flows involving large coherent structures, we have to infer the pressure distribution using assumed simplified relationships between velocity and pressure, e.g. a Rankine vortex, which at best provides some qualitative insight.

This lack of adequate capability to determine the spatial pressure distribution, and the need of experimental data for both cavitation and turbulence research provide the motivation for the present on-going effort. We have developed a system that is capable of measuring the instantaneous pressure distribution in a non-intrusive manner based on particle image velocimetry (PIV) technology (Liu and Katz, 2003 and 2004). In particular, this system utilizes four-exposure PIV to measure the distribution of material acceleration, and then integrates it to obtain the pressure. This approach provides the instantaneous pressure, material acceleration and velocity distributions simultaneously.

The material or Lagrangian acceleration has been studied both numerically and experimentally before. The objectives of most of previous works have been either to provide data for Lagrangian stochastic turbulence models (Yeung 2001, 2002; Vedula and Yeung 1999; Voth *et al* 1998; La Porta *et al* 2001; Ott and Mann 2000), or to develop techniques for acceleration measurements (Jakobsen *et al* 1997; Dong *et al* 2001; Christensen and Adrian 2001, 2002). Voth *et al* (1998) and La Porta *et al* (2001) tracked and calculated the acceleration of individual particles. Ott and Mann (2000) used four synchronized CCD cameras to track the trajectories of seed particle pairs and investigated their diffusion characteristics in a turbulent flow generated by two oscillating grids. Jakobsen *et al* (1997) utilized a specially designed four-CCD camera system to obtain the acceleration field near the wall of a surface wave flume based on PIV technology. They validated their acceleration measurement by integrating the averaged acceleration, and then comparing it to the mean pressure difference between two wall pressure taps. Dong *et al* (2001) obtained two-dimensional Eulerian acceleration distributions using one CCD camera by combining cross-correlations and autocorrelations on two successive, doubly exposed frames. The two instantaneous velocity fields, each obtained from the auto-correlation analysis, were used for computing the acceleration. Christensen and Adrian (2001, 2002) measured the instantaneous Eulerian acceleration field of a boundary layer flow by using two CCD cameras with cross-polarized laser beams as light sources. They also calculated the so-called velocity bulk-convective-derivative field, and concluded that the dominant vortical structures remained almost frozen in time. Sridhar and Katz (1995) used triple exposure images to simultaneously measure the velocity and material acceleration of microscopic bubbles and the fluid surrounding them. These studies did not attempt to measure the pressure distributions, and did not have the resolution needed for such measurements.

In our previous papers (Liu and Katz, 2003 and 2004), we introduced the principle of the PIV based material acceleration and pressure measurement technique, demonstrated the validity of the technique using synthetic images and presented preliminary results of pressure distribution measurements in a cavity flow. As we implemented the technique, we have encountered a series of problems that affected the uncertainty in the measurements. In this paper, we introduce solutions to these problems, including substantially improved techniques for matching images recorded by different cameras, and for integrating the material acceleration. To provide a complete picture, we start by introducing the principles of the new technique, some of which has already appeared in our previous papers.

2
Measurement of pressure distribution by integrating the material acceleration

Based on the Navier-Stokes equation, the pressure gradient can be expressed as

$$\nabla p = -\rho \left(\frac{D\vec{U}}{Dt} - \nu \nabla^2 \vec{U} \right) \qquad (1)$$

Thus, if both of the material acceleration, $D\vec{U}/Dt$, and the viscous terms $-\nu \nabla^2 \vec{U}$ can be measured directly, the pressure p can be integrated using equation 1. In a high Reynolds number flow field located away from boundaries, the material acceleration is dominant and the viscous term is negligible. For example, in a turbulent near-wake experiment Liu (2001) and Thomas and Liu (2004) found that the Reynolds-averaged viscous term is 10^{-5} times smaller than the streamwise acceleration term. In an experimental investigation of the acceleration correlations for locally isotropic turbulence, Hill and Thoroddsen (1997) also concluded that for large Reynolds numbers, the two point correlation of acceleration is dominated by the two point correlation of the pressure gradient, rather than the viscous term. However, one should be careful to evaluate the contribution of the viscous term, and avoid integrating along a boundary layer. Neglecting the viscous term (requires verification), one has to measure the material acceleration and integrate it to determine the pressure.
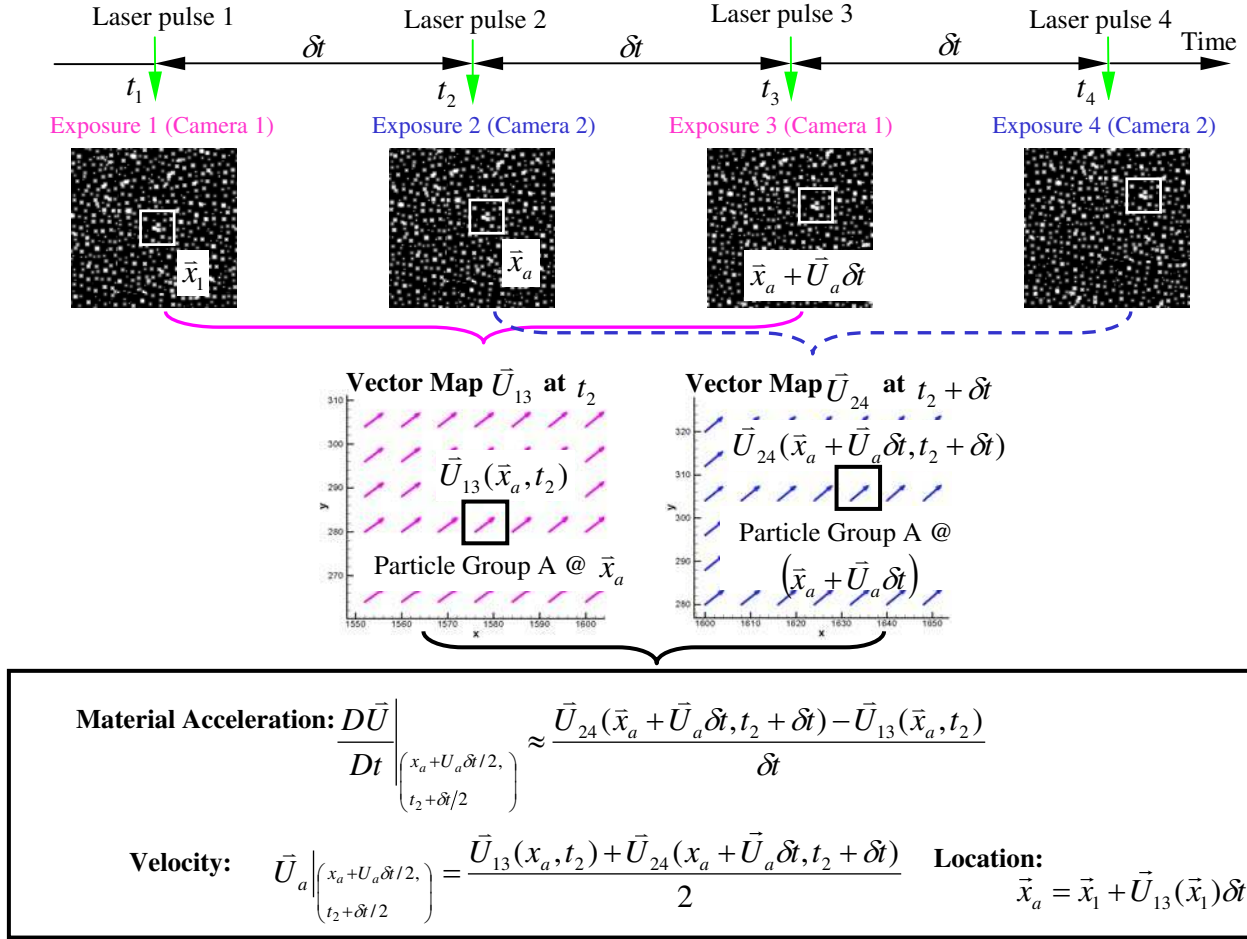
Figure 1. Schematic illustration of the material acceleration measurement technique.

   The present technique for measuring the material acceleration is based on its definition, while considering the inherent properties of PIV, which measures the instantaneous velocity from the displacement of a group of particles. To measure the material acceleration, one has to compare the velocity of the same group of particles at two different times. The principles of the present approach are illustrated in Figure 1. We use a four-exposure PIV system with two "cross-correlation" cameras to record four exposures of the particle traces within the sample area. The timings of the laser sheet pulses are denoted as t_1, t_2, t_3 and t_4, and there is an equal time interval, δt, between them. Each image is recorded on a separate frame. Camera 1 records images 1 and 3, and the data are used to determine the first velocity distribution, $\bar{U}_{13}$. Camera 2 records images 2 and 4, which are used for calculating the second velocity map, $\bar{U}_{24}$. Since intrinsically, cross-correlation PIV analysis tracks the displacement of the same group of seed particles between exposures, the local velocity determined by exposures 1 and 3 can be used to estimate the location of the same particle group during exposure 2. Similarly, the local velocity determined by exposures 2 and 4 can be used to estimate the location of the same particle group during exposure 3. Thus, a particle group located at $\vec{x}_a$ when $t = t_2$ has a velocity $\bar{U}_{13}(\vec{x}_a)$. At $t_2+\delta t$ (i.e. at t_3), the same particle group is located at $\vec{x}_a + \vec{U}_a\delta t$, where

$$\vec{U}_a(\vec{x}_a+\vec{U}_a\delta t/2, t_2+\delta t/2) = \tfrac{1}{2}(\vec{U}_{13}(\vec{x}_a,t_2)+\vec{U}_{24}(\vec{x}_a+\vec{U}_a\delta t,t_2+\delta t)) \quad (2)$$

is the averaged Lagrangian velocity between t_2 and $t_2+\delta t$. This implicit expression requires iterations during data analysis. As a first approximation we typically choose $\vec{U}_a^1 \approx \tfrac{1}{2}(\vec{U}_{13}(\vec{x}_a,t_2)+\vec{U}_{24}(\vec{x}_a,t_3))$ and then iterate to determine the correct value. Typically, about two iterations are sufficient to obtain a value that is less than the PIV uncertainty

level from the asymptotic value. The material acceleration at $\bar{x}_a + \bar{U}_a \delta t / 2$ and $t = t_2 + \delta t/2$, determined by tracking a group of seed particles, can then be estimated as:

$$\left. \frac{D\bar{U}}{Dt} \right|_{\substack{\bar{x}_a + \bar{U}_a \delta t / 2 \\ t_2 + \delta t/2}} \approx \frac{\bar{U}_{24}(\bar{x}_a + \bar{U}_a \delta t, t_2 + \delta t) - \bar{U}_{13}(\bar{x}_a, t_2)}{\delta t} \qquad (3)$$

The (time) averaged Eulerian velocity distribution at the same time can be calculated by averaging the two vector maps, i.e.

$$\bar{U}(\bar{x}, t_2 + \delta t / 2) \approx \tfrac{1}{2}(\bar{U}_{1-3}(\bar{x}, t_2) + \bar{U}_{2-4}(\bar{x}, t_3)) \qquad (4)$$

Integrating the material acceleration from a reference point with known pressure provides the pressure distribution $p(\bar{x}, t_2 + \delta t / 2)$, as long as the viscous terms are small. Using 2-D PIV, the measurments provide only two components of the velocity and material acceleration. At least two of the three components of the viscous term can also be evaluated, mostly to insure that they are small. Evaluation of data involving a free shear layer indeed confirms that the viscous terms are several orders of magnitude smaller than the acceleration. Note, the procedure described here assumes that the particles remain within the laser sheet as the four exposures are recorded. Calculating the first velocity field using exposures one and three ($\bar{U}_{13}$) and the second field using exposures two and four ($\bar{U}_{24}$) improves the chances that we indeed follow the same group of particles. For example, to obtain the velocity from exposure one and three, the same particles have to remain in the sample area, i.e. they are also there during exposure two. The same applies to the second set. Low correlation values, which are regularly checked, are reliable indicators for effects of out-of-plane motion. Adjustment of the delay between exposures and of the laser sheet thickness can be used for addressing such cases.

In the following section we implement this procedure to calculate the pressure distribution in synthetic flow fields, and compare the computed and previously known pressure distributions. Note that if 3-D data is available, e.g. from holographic PIV, the acceleration can also be calculated using an Eulerian approach. In this case, one can calculate the local unsteady and convective terms of the acceleration at the same location.
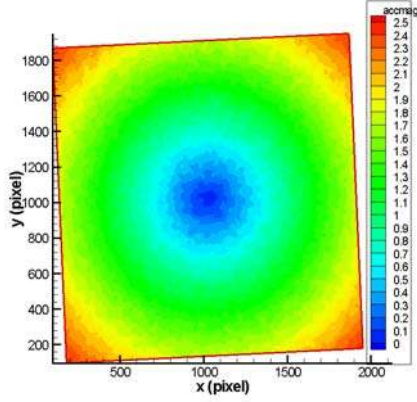
3
Proof of concept tests

To validate the principles of the pressure measurement technique, we use synthetic images of solid-body rotation and stagnation point flows. The simulated seed particles are distributed homogeneously in a 2048×2048 pixels image using a random number generator available in Matlab. The particle concentration is set to maintain an average of 25 particles per interrogation window of 32×32 pixels. The particle size has a Gaussian distribution, with a mean diameter of 2.4 pixels and a standard deviation of 0.8 pixels. The intensity is also Gaussian distributed, with a peak grayscale of 240. Based on the first synthetic image, the subsequent three planes are generated by displacing the particles according to the local theoretical velocity, using the analytical expressions for the velocity fields.

The selected rotation rate of the solid-body-rotation flow is $\omega = 0.0625$/sec, and the constant strain rate for the stagnation point flow is $S = 0.025$/sec. The time interval between exposures is $\delta t = 0.5$ sec. For each set of four images we calculate two velocity fields, $\bar{U}_{13}$ and $\bar{U}_{24}$ using an in-house developed PIV code. Its widely used version is described in Roth *et al* (1999, 2001), and a recent, substantially more accurate technique is presented in Chen and Katz (2005). Using these velocity distributions, we calculate the instantaneous material acceleration and then integrate it to obtain the pressure, following the procedures described in the previous section.
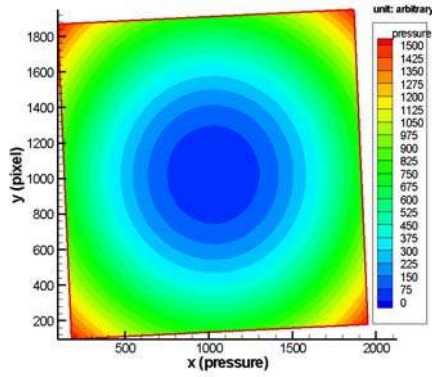
Figure 2(a) shows the material acceleration magnitude for the solid-body rotation. Note that since the material acceleration is evaluated at $t = t_2 + \delta t/2$, the grid shown in Figure 2(a) is rotated (distorted). The pressure field shown in Figure 2(b) is rotated accordingly. The irregularities in Figure 2 (a) are caused by errors that can be traced to the inherent uncertainty of the PIV analysis, and the truncation error of the finite difference scheme. These errors contaminate the calculated pressure and their effects must be minimized. Since pressure is a scalar field, the integration of pressure gradients must be independent of the integration path. To minimize the effect of the acceleration error, we implement a method featuring averaged, shortest path, virtual boundary, omni-directional integration over the entire flow field, which will be discussed in detail in Section 6. Unlike the acceleration, the irregularities disappear in the pressure distribution contours due to the omni-directional integration that acts as a low-pass filter. The measured radial pressure distribution is compared to the theoretical values in Figure 3(a). The
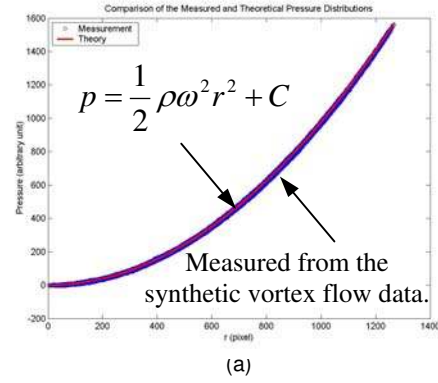
Magnitude of Material Acceleration

(a)

$$p = \frac{1}{2}\rho\omega^2 r^2 + C$$

Measured from the synthetic vortex flow data.

(a)

Spatial Pressure Distribution

(b)

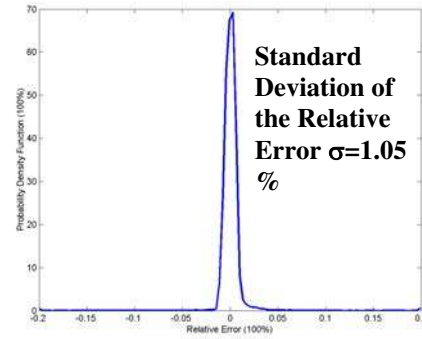**Standard Deviation of the Relative Error σ=1.05%**

(b)

Figure 2. (a) Magnitude of the material acceleration and (b) spatial pressure distribution integrated from the material acceleration for the synthetic rotational flow.

Figure 3. (a) Radial pressure distribution and (b) probability density function of the relative error of pressure for the synthetic rotational flow.

degree of agreement is self-evident. The probability density function of the relative error of the pressure measurement, presented in Figure 3(b), has a standard deviation of 1.05%.

In addition to the synthetic rotational flow, we also applied the procedures to the synthetic stagnation point flow. In this case, the standard deviation of the relative error of the measured pressure from the exact value is 1.03%, roughly the same as that of the rotational flow. Note that in our previous papers (Liu and Katz, 2003 and 2004), the standard deviations of the relative pressure error for the synthetic rotational and stagnation point flows are 1.7% and 2.3%, respectively. The current lower level of accuracy is achieved by applications of an improved pressure integration algorithm (see Section 6) and an improved PIV analysis code, which eliminates the peak-locking effect by implementing the correlation mapping method (Chen and Katz 2005) together with particle image distortion corrections (Huang *et al* 1993).

4
Experimental and optical setup

The pressure measurement technique is applied to a cavity shear flow in a small water tunnel, which is described in Gopalan and Katz (2000). The optical setup is sketched in Figure 4, and the test model in Figure 5. The 38.1mm long, 50.8mm wide and 30.0mm deep 2-D cavity is installed in the 50.8×63.5 mm test section. As shown, the test model has a contraction ramp leading to the cavity, and a diffusing ramp downstream of the cavity. A 13mm long region with tripping grooves having a notch depth of 0.46mm and opening of 1.00mm is machined at the beginning of the contraction ramp in order to trip the boundary layer. Figure 5 also shows the locations of three pressure transducers, which are needed for calibration. One transducer is installed upstream of the cavity; the second is located at the bottom of the cavity, and the third is installed on the downstream face of the cavity, just below the corner. Custom polymer coated, Endevco 8510B-5, miniature, piezoresistive pressure transducers are currently
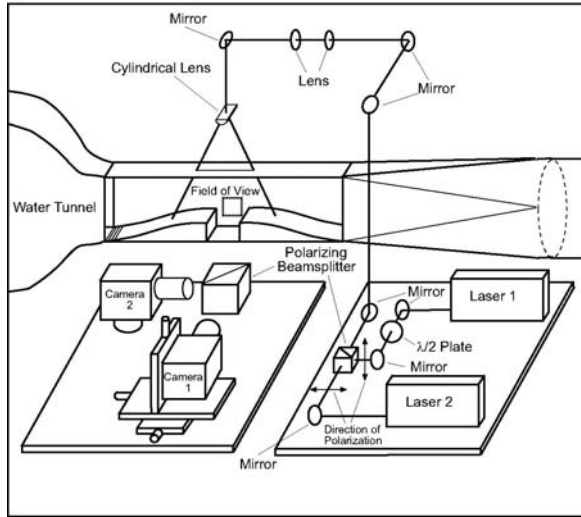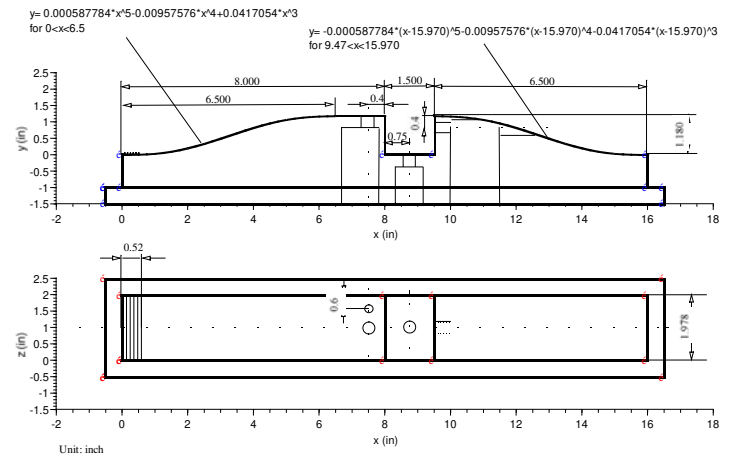
Figure 4. Optical set-up.

Figure 5. Experimental body for cavity shear flow.

being used. These transducers are fragile, and fail after few months of operation, but they are the only ones available with the required combination of resolution, sensitivity, small size and ability to operate in water. Earlier attempts to use miniature piezoelectric transducers (PCB 105B02) were abandoned due to response of the transducer to direct illumination by the laser.

To record the four exposures we use two 2K×2K "cross-correlation" digital cameras with interline image transfer (Kodak ES4.0). Images 1 and 3 are recorded by camera 1, and images 2 and 4 are recorded by camera 2. The light sources are two dual-head Nd:Yag lasers, with flashes 1 and 3 generated by laser No. 1, and flashes 2 and 4 generated by laser No. 2. A half-wave plate is used for rotating the polarization of laser No. 1 before mixing the beams and expanding them to sheets. Consequently, the polarization direction of the light in pulses 1 and 3 is perpendicular to that of pulses 2 and 4. As discussed in Christensen and Adrian (2002), most of the light reflected from tracer particles (hollow, 8-12μm, glass spheres with specific gravity of 1.05-1.15) located within the laser sheet maintains its polarization angle. Thus, by placing a polarizing beam splitter (cube) in front of the cameras, we can separate images 1 and 3 from images 2 and 4, and direct them onto their respective cameras. The interline transfer feature of the cameras enables recording of each image on a separate frame.

5
Vector alignment based on local deformation correction

It is essential to match the field of views of the two cameras, requiring an elaborate alignment and calibration process. As a result, camera 1 is installed on a three-axis translation stage, while camera 2 is installed on a tilt and rotation stage (see Figure 4). A target with grid (Edmund Industrial Optics, model NT46-250), illuminated using incandescent light source, is placed in the test section. The plane of the target is aligned with the laser sheet to the best of our ability, considering that the sheet has a finite depth. The images of this target, as recorded by the two cameras, are compared to each other, and the differences between them are minimized by iteratively adjusting the focus of the lens and the settings of mounting stages.

Due to limitations of the mechanical alignment mechanism, no matter how much care is taken, it is virtually impossible to perfectly coincide the laser sheet with that of the target. Furthermore, differences in orientation and location of the two cameras cause location dependent shifts, whereas unavoidable lens-induced distortions cause location dependent variations in magnification. For the 25.4× 25.4mm field of view of a 2K× 2K camera, a 0.05 mm misalignment in lateral direction in the target plane results in a 4 pixels displacement on the image plane, which further corresponds to an acceleration error of 40,000m/s^2, an unacceptable level. To overcome this problem, subsequent to the mechanical adjustments, we also compare images recorded by the two cameras of a laser sheet densely seeded with particles. These images are acquired at the same time by triggering both lasers simultaneously, with no flow in the test facility. Using cross-correlation analysis, similar to typical PIV procedures, we determine the spatial distribution of relative displacement between the two images. An example is presented in Figure 6. Based on this relative displacement map, one can align velocity vectors obtained by one camera to the other using three different methods:
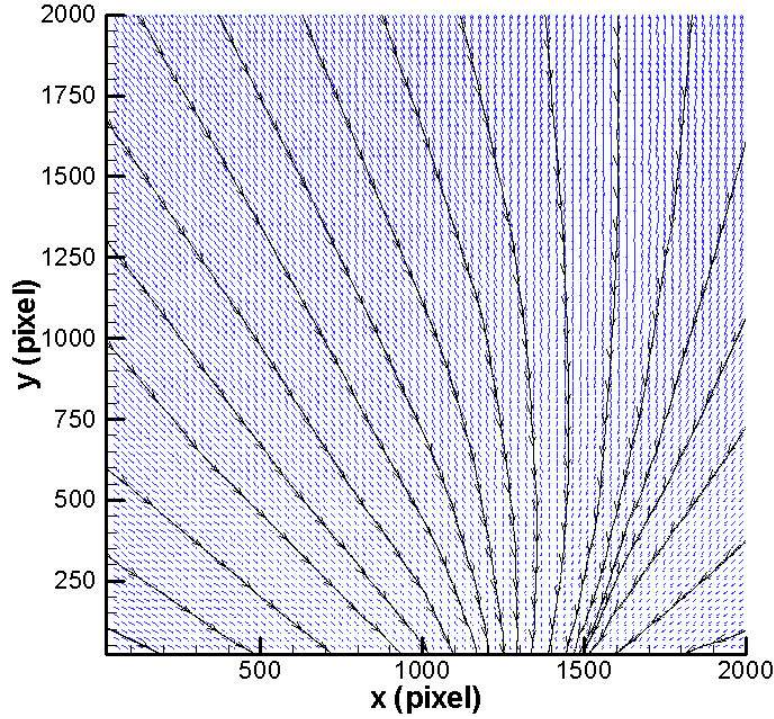
Figure 6. A sample displacement vector map obtained by cross-correlating images recorded by cameras 1 and 2 of the same particle filed simultaneously with no flow.

Method 1, Decomposition of Camera Image Relative Displacement: For the most part, the relative displacement can be decomposed into relative translation, rotation and magnification difference between the two cameras. Using the resulting parameters, vector maps obtained by camera two are aligned with and adjusted to those obtained by camera one. This is the method used in Liu and Katz (2003 and 2004). Following these corrections, the resulting vector maps contain mostly errors due to lens-induced distortion. For a while we assumed that this approach will provide sufficient corrections, but discovered that the distortion introduced sufficient bias to create unacceptable errors in pressure.

Method 2, Global Mapping for Velocity Vector Alignment: The next approach was an attempt to generate global mapping functions, typically polynomials of different orders, for the spatial distributions of velocity vector alignments. Taylor expansion was then used for determining local relationship between vectors on the two frames, which was then used for adjusting the vectors of camera two to that of camera one. In spite of considerable effort, this approach also failed due to the inability of the global functions to accurately describe the local deformations.

Method 3, Local Deformation Correction for Vector Alignment: Using Taylor expansion, the velocity vectors obtained by the two cameras can be aligned using an expression involving the local spatial derivatives of the camera image relative displacement, e.g., the sample vector map shown in Figure 6. This is the best method among the three, and the improvements are substantial, by almost an order of magnitude, especially if performed using a recently introduced PIV analysis technique (Chen and Katz, 2005) that overcomes the peak locking bias that plagues all the typical sub-pixel-fitting codes. This method solved our problem, and as a result, it is explained in detail below.

As illustrated in Figure 7, slight mismatches in location, magnification and deformation in the images recorded by cameras 1 and 2 will cause differences in the measured velocity vectors. Suppose $O(x_0, y_0)$ and $P(x, y)$ are the starting and ending points of a vector $\overrightarrow{OP}$ on camera 1, where $\overrightarrow{OP} = (x - x_0, y - y_0) = (u_{c1}, v_{c1}) = \vec{V}_{C1}$. Correspondingly, the same vector on camera 2 is denoted as $\overrightarrow{O'P'} = (x' - x_0', y' - y_0') = (u_{c2}, v_{c2}) = \vec{V}_{C2}$, with $O'(x_0', y_0')$ and $P'(x', y')$ being the starting and ending points, respectively. The relative displacement between $O(x_0, y_0)$ and $O'(x_0', y_0')$ can
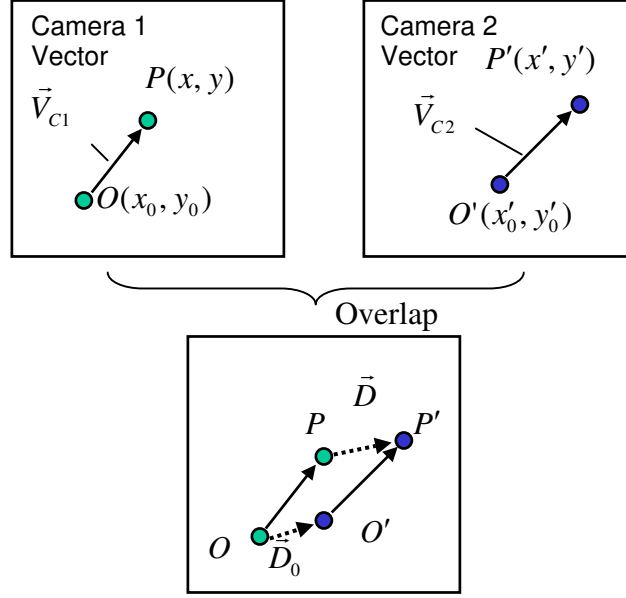
Figure 7. Schematic illustration of two velocity vectors, which are supposed to be identical, but are different due to mismatches in location, magnification and deformation in the images recorded by camera 1 and camera 2.

be denoted by $\vec{D}_0 = (D_{x0}, D_{y0})$. Similarly, $\vec{D} = (D_x, D_y)$ denotes the relative displacement between $P(x, y)$ and $P'(x', y')$. Thus,

$$x'_0 = x_0 + D_{x0} \qquad (5)$$

$$y'_0 = y_0 + D_{y0} \qquad (6)$$

$$x' = x + D_x \qquad (7)$$

$$y' = y + D_y \qquad (8)$$

With Taylor expansion of D_x, one obtains

$$x' - x'_0 = (x + D_x) - (x_0 + D_{x0})$$
$$= (x - x_0) + (x - x_0)\frac{\partial D_x}{\partial x}\bigg|_{x_0,y_0} + (y - y_0)\frac{\partial D_y}{\partial y}\bigg|_{x_0,y_0} + \frac{1}{2}\left[(x - x_0)^2\frac{\partial^2 D_x}{\partial x^2}\bigg|_{x_0,y_0} + 2(x - x_0)(y - y_0)\frac{\partial^2 D_x}{\partial x \partial y}\bigg|_{x_0,y_0} + (y - y_0)^2\frac{\partial^2 D_x}{\partial y^2}\bigg|_{x_0,y_0}\right] + H.O.T. \qquad (9)$$

i.e.,

$$u_{c2} = u_{c1} + u_{c1}\frac{\partial D_x}{\partial x}\bigg|_{x_0,y_0} + v_{c1}\frac{\partial D_y}{\partial y}\bigg|_{x_0,y_0} + \frac{1}{2}\left[u_{c1}^2\frac{\partial^2 D_x}{\partial x^2}\bigg|_{x_0,y_0} + 2u_{c1}v_{c1}\frac{\partial^2 D_x}{\partial x \partial y}\bigg|_{x_0,y_0} + v_{c1}^2\frac{\partial^2 D_x}{\partial y^2}\bigg|_{x_0,y_0}\right] + H.O.T. \qquad (10)$$

where u represent the horizontal velocity component, and the subscription $C1$ and $C2$ denote the cameras 1 and 2, respectively. Similarly, we get

$$v_{c2} = v_{c1} + u_{c1}\frac{\partial D_y}{\partial x}\bigg|_{x_0,y_0} + v_{c1}\frac{\partial D_y}{\partial y}\bigg|_{x_0,y_0} + \frac{1}{2}\left[u_{c1}^2\frac{\partial^2 D_y}{\partial x^2}\bigg|_{x_0,y_0} + 2u_{c1}v_{c1}\frac{\partial^2 D_y}{\partial x \partial y}\bigg|_{x_0,y_0} + v_{c1}^2\frac{\partial^2 D_y}{\partial y^2}\bigg|_{x_0,y_0}\right] + H.O.T. \qquad (11)$$

Using expressions (10) and (11), the camera 1 velocity vector components can be aligned to the scale and orientation of camera 2, provided the distributions of $\vec{D}(x, y)$ and its derivatives are known. Accurate distributions of $\vec{D}(x, y)$ are provided by cross-correlating images of the same particle field at the same time, e.g. Figure 6.

	Mean δu (pixel)	Mean δv (pixel)	Standard deviation of δu (pixel)	Standard deviation of δv (pixel)
Decomposition of camera image relative displacement	-0.153	0.229	0.169	0.206
6th order polynomial global mapping	-0.00076	0.00111	0.078	0.078
1st order local deformation correction using code of Roth and Katz (2001)	-0.00046	0.00099	0.0613	0.0682
2nd order local deformation correction using code of Roth and Katz (2001)	-0.0016	-0.0005	0.0625	0.0688
1st order local deformation correction using code of Chen and Katz (2005)	0.00066	-0.00048	0.0112	0.0109
2nd order local deformation correction using code of Chen and Katz (2005)	-0.00029	-0.00017	0.0107	0.0105

Table 1. Comparison of accuracy of velocity vector alignment methods based on distorted synthetic images.

6th order Polynormial Global Mapping

2nd order local deformation correction using standard PIV code (Roth and Katz 2001)

2nd order local deformation correction using new CMM code (Chen and Katz 2005)
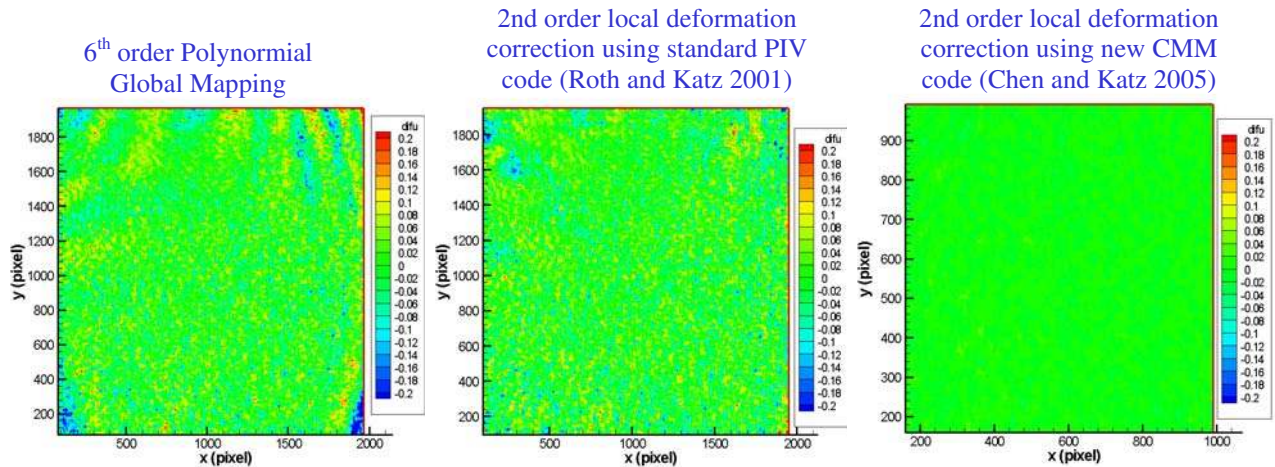

Figure 8. Comparison of spatial distribution of the horizontal-component error of the corrected/aligned vectors of distorted synthetic images.

Following these corrections, the resulting vector maps contain mostly errors due to lens-induced distortion of one camera. However calibrations using the target show that this distortion is less than 0.003 pixel per pixel, much smaller than the typical accuracy of the PIV cross-correlation analysis (on the order of 0.1 pixel). Consequently, the effect of image distortion imbedded in the velocity is not a primary concern, at least for our present setup.

To gauge the accuracy of the above three velocity vector alignment methods, we distorted a pair of synthetic images using two sets of spatial distortion function, based on measured calibration images of a grid target. The velocity vectors of these distorted images were then corrected using the above three alignment methods. The statistics of the velocity difference after the alignment is listed in Table 1. Decomposition of the camera image relative displacement introduces a large and unacceptable level of error, while the 2nd order local deformation correction, together with the PIV analysis code based on the correlation mapping method (abbreviated as CMM, see Chen and Katz, 2005), gives the most accurate alignment result.

Another demonstration of the improvements is presented in Figure 8. Although the standard deviation of the 6th order polynomial mapping and that of local deformation with the standard PIV code (Roth, 1998; Roth and Katz 2001) are very similar, the 6th order polynomial fit introduces a larger bias in pressure due to the more regular
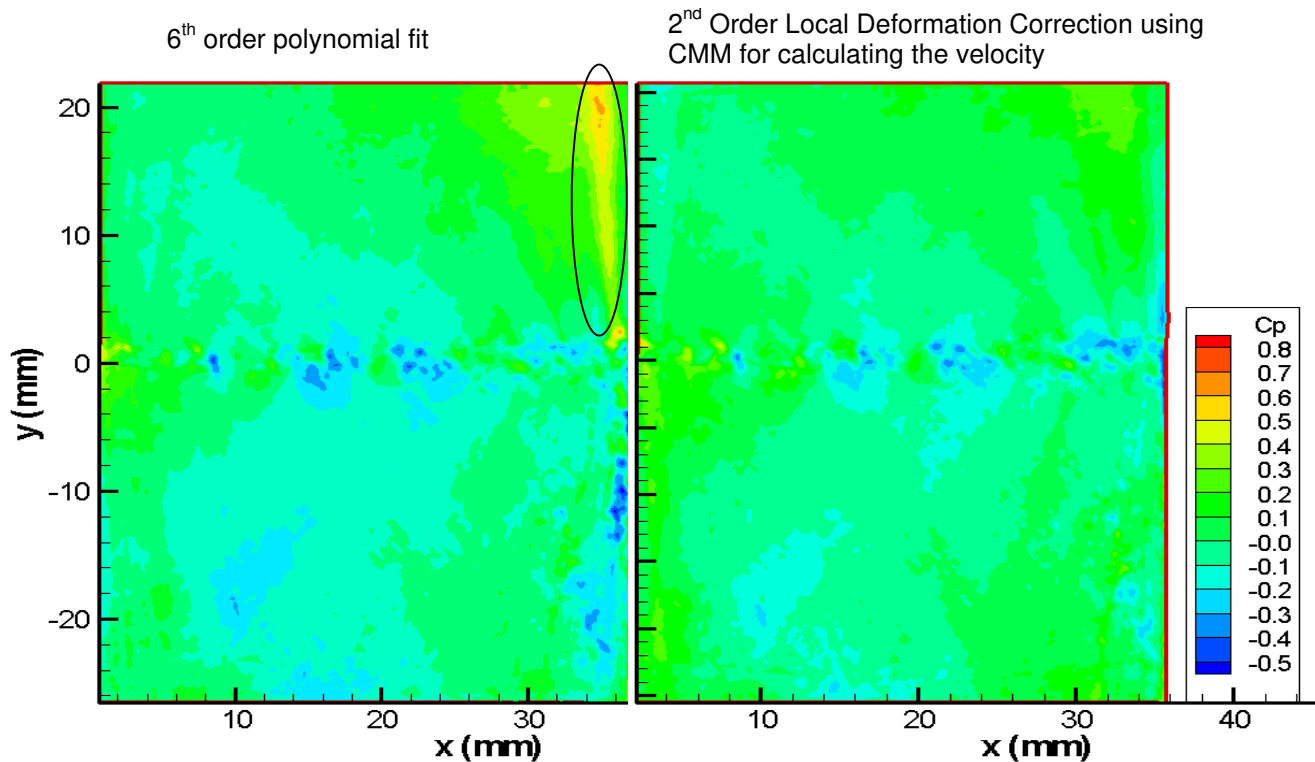
Figure 9:   A comparison between pressure distributions calculated using the same data, but different methods for matching the two fields of view. Left: matching by polynomial fit; right: Matching by 2nd order local deformation correction using the CMM PIV method. Bias errors of the 6th order polynomial fit generate unphysical pressure gradients above the shear layer.

pattern. However, both represent unacceptable level of mismatch between frames. The 2nd order deformation correction using the CMM code represents an improvement of almost an order of magnitude, and *the problem of matching the two frames has been solved*. To illustrate the impact of the new procedures on the pressure distributions, Figure 9 compares the instantaneous pressure distributions of the cavity shear layer calculated using the same velocity data, but different methods for matching the two fields of view. The distribution calculated using the 6th order polynomial fit (left side) clearly displays unrealistic pressure peaks above the shear layer, especially along the upper right side of the distribution. The high negative peaks along the right cavity wall below the shear layer is also unrealistic, considering the magnitudes of velocity there. The origin of this error can be traced directly to the bias introduced by the sixth-order polynomial fit to match the two fields of view. This bias disappears when we use 2nd order local deformation correction.

6
Pressure integration algorithm

With the material acceleration measured at discrete nodal points in a planar flow field, the pressure can be reconstructed by solving a least square problem. For a sample grid, at each nodal point there are two known components of the material acceleration, and one unknown variable, the pressure. These known and unknown variables are related to each other via discrete differential equations based on the Navier-Stokes equation, and form an over-determined matrix equation. The three primary ways to solve this matrix equation are: matrix iteration (Southwell 1980), direct matrix inversion (Herrmann 1980) and singular value decomposition (Press *et al* 2002). However, the matrix iteration method results are sensitive to the initial value setting, and use of a relaxation factor requires experience. The direct matrix inversion and singular value decomposition approaches must involve the full matrix during computation. For a grid with 220×220 nodes, which is typical for PIV analysis by using 2K×2K cameras, the largest storage requirement of a full matrix is 37 gigabytes, which is impractical at the current level of computer technology. To bypass these limitations, we developed algorithms for direct acceleration integration.
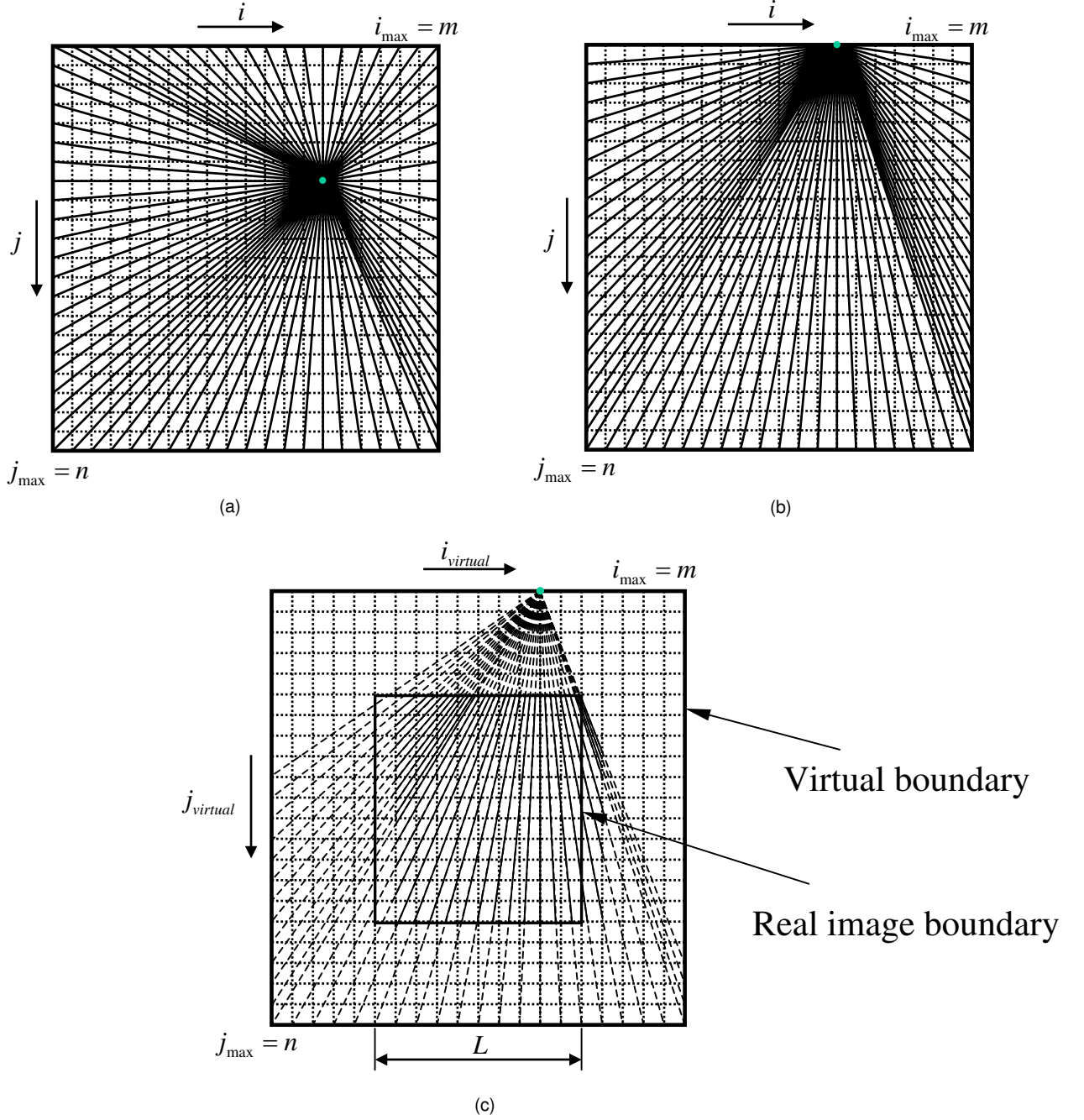
(a)

(b)

(c)

Figure 10. Pressure gradient integration methods: (a) averaged, shortest path, omni-directional integration; (b) a method equivalent to (a) but with higher efficiency; (c) virtual boundary omni-directional integration method.

Since pressure is a scalar field, the integration of pressure gradients must be independent of the integration path. To minimize the effect of acceleration error, we first implemented a method featuring *averaged, shortest path, omni-directional integration* over the entire flow field. An illustration of the integration paths used initially is presented in Figure 10(a). Starting from the top left corner, we first integrate the acceleration along the boundary. To determine the pressure at a certain internal point, we then integrate the acceleration along nearly straight paths (shortest paths) from each of the boundary point to the internal node, and then average all the integration results. For an $m \times n$ grid, the number of boundary nodes is $2(m+n)$. Thus, the total number of integration paths needed for calculating the pressure over the entire domain is $2(m+n)mn$. For $m = n = 250$, the number of paths is 62.5×10^6. Such a large number is prohibitively expensive, especially considering that one may wish to perform thousands of measurements to obtain converged statistics on the pressure field and pressure-velocity correlations.
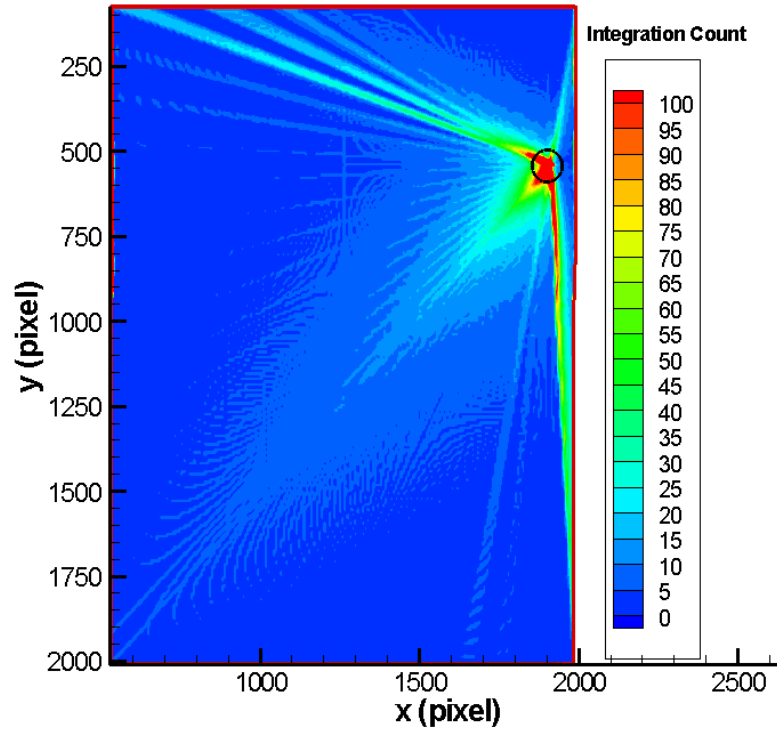
11

Figure 11. Distribution of the number of times a certain node is used for calculating the pressure at the encircled node. For points located near the center of the sample area, the distribution is uniform. For points located near the boundary, the distribution is not uniform.

(a)   (b)
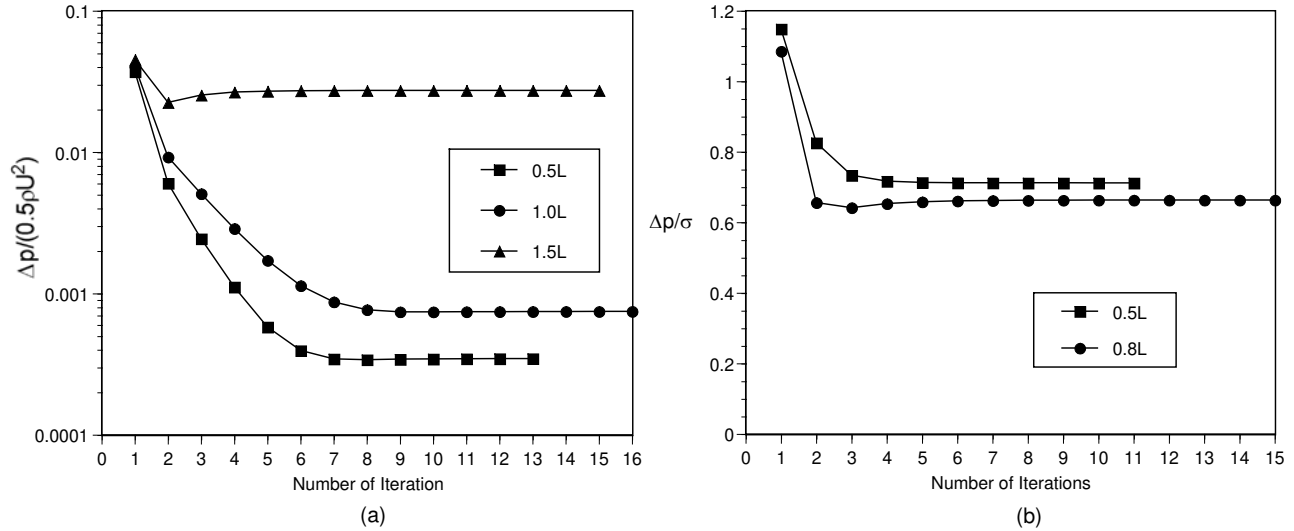
Figure 12. Convergence test for virtual boundary iteration algorithm. (a) Cavity shear flow; (b) Simulated rotational flow.

To solve this problem, we proposed an equivalent, but more efficient, *modified omni-directional integration* algorithm, as illustrated in Figure 10 (b). Instead of focusing on the internal nodes, we focus on the boundary, and integrate from *each* of the boundary node to *all the other* boundary nodes. As the integration path crosses a certain internal node, the result of integration is stored in a data bin associated with this node. Repeating this procedure for all the boundary nodes results in multi-direction integration for each internal node. This process substantially reduces redundant integration paths. The total number of integration paths for an $m \times n$ grid is reduced to $2m(2n+m)+2n(2m+n)$, i.e. 0.75×10^6 for $m=n=250$, almost two orders of magnitude less than the original procedure. Implementing this method using a single processor, mid-range Pentium PC provides the pressure
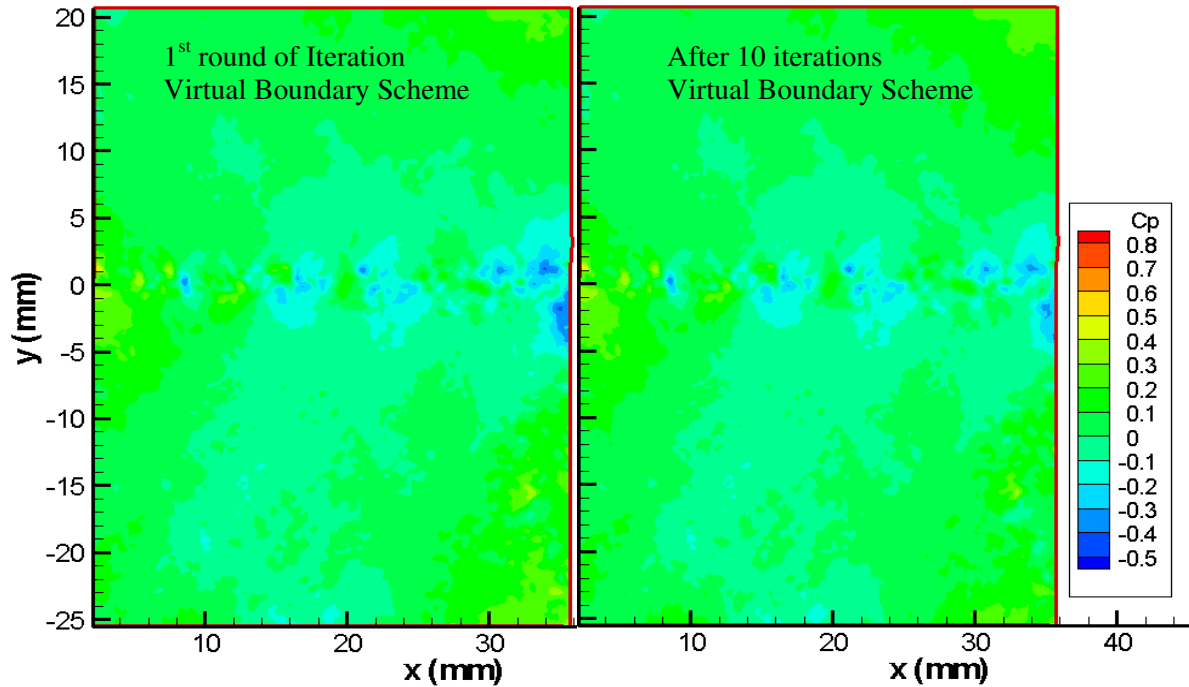
Figure 13: The pressure distribution computed using an extended virtual boundary and iterations to correct the boundary values along the perimeter of the sample area.

distribution in about four minutes - not yet an optimum (<1 min is desirable), but already manageable. We had used this procedure for a while, but then realized that we have to resolve two major problems, as described below.

First, as illustrated in Figure 11, the number of times a certain node is crossed during the omni-directional integration is not uniform in the circumferential direction, and varies depending on location in the sample area. Integration to nodes located close to the center will give similar weight to all directions, while integration to nodes located near the boundaries, as shown, involves non-uniform utilization of integration paths. Errors and bias would be an inherent outcome.

The second problem is the weight given to boundary nodes. The velocity in boundary points is typically the least accurate primarily due to the higher image deformation along its edges. Since each integration path starts at the boundary, the boundary error adversely affects all the data.

To solve these problems, we have introduced the *virtual boundary integration method*, which is illustrated in Figure 10 (c). The integration still starts from and stops at the real boundaries, but instead of following paths originating from real boundaries, this time the integration proceeds along paths originating from the extended virtual boundaries with some distance apart from the real boundaries. Consequently, all the nodal points of interest are now located away from the boundary, preventing the path clustering shown in Figure 11.

Furthermore, and equally important, we no longer have rely on accurate integration along the perimeter to obtain the pressure along the boundary. We still integrate along the perimeter initially, but since each boundary node is crossed by numerous paths, the initial value can be corrected/replaced with the results of the omni-directional integration, greatly reducing the effect of errors in the initial integration along the boundary. The entire process can then be repeated until the results converge or the variations between iterations decrease to below an acceptable threshold level. The number of iterations required to obtain converged results is indicated in Figure 12 (a) as a function of the gap between the real and virtual boundaries. The gap is expressed in terms of L, a characteristic length of the real grid size. For the experimental data of the cavity shear flow, the initial variations between iteration steps (residue error) is less than 5% of the dynamic head, but it decreases to less than 0.04% of the dynamic pressure after 7 iterations for a gap of $0.5L$. As is evident, the number of iterations required to obtain converged results decreases with increasing gap. This is due to the fact that the arrangement of the integration paths is equivalent to allocation of directional dependent weight to the multi-directional integration. With increasing gap between virtual and real boundaries, the weight allocation becomes more balanced, achieving a quicker rate of convergence. Though resulting in a quicker convergence, the more balanced weight arrangement with increasing gap may not necessarily guarantee a better data involvement and thorough mixing during integration, and may even result in more residue
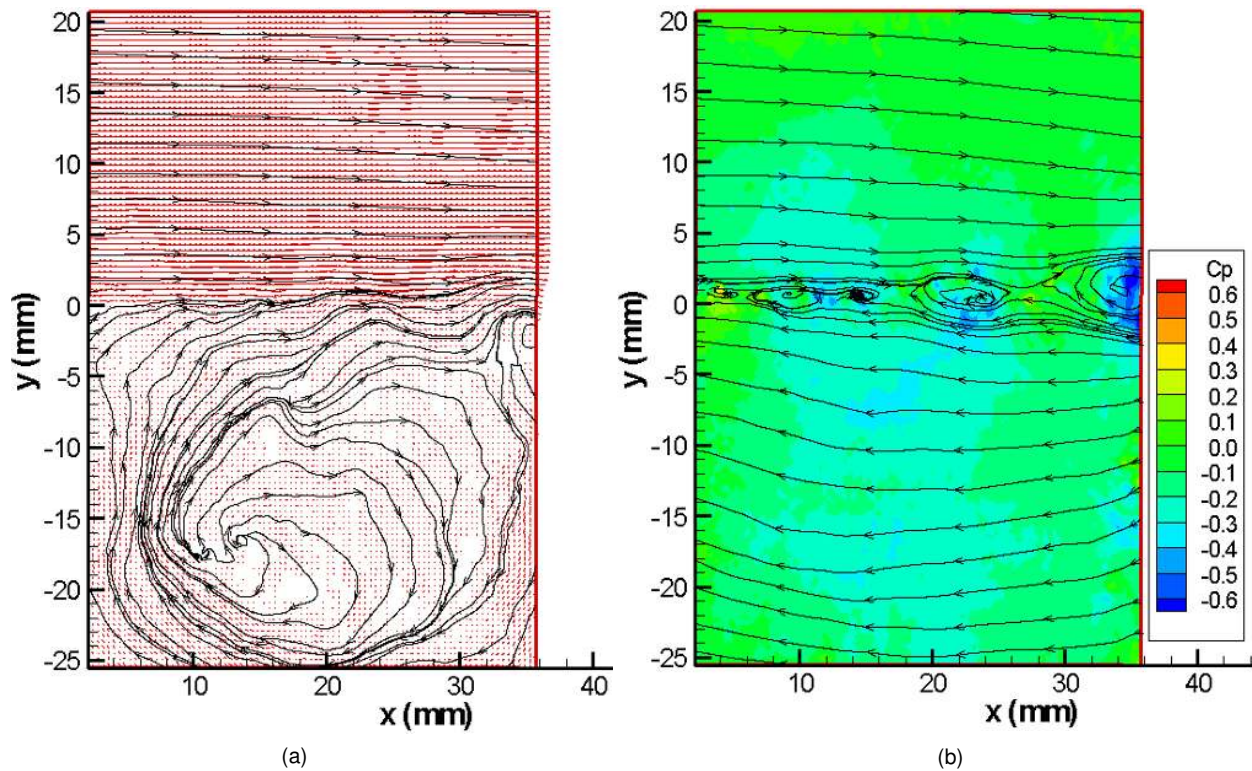
13

Figure 14. Sample results for cavity shear flow at U_e=10 m/s and Re=335,000. (a) Instantaneous streamlines ; (b) Instantaneous pressure distribution with streamlines based on a new reference frame moving downstream at half of Ue to show the pseudo vortical structure.

error. It seems that the optimum gap is somewhere in the $0.5L \sim 1.0L$ range. However, we need to gain more experience in order to identify an optimum.

For the simulated rotational flow based on synthetic images shown in Figure 12(b), at convergence Δp, the averaged pressure difference between iterations, is only about 0.7 of σ (=1%), the standard deviation of the relative error in the measured pressure. Thus, the convergence level is quite satisfactory. The relative quicker convergence for the simulated rotational flow is due to its more homogeneous error distribution than that of the cavity shear flow.

The impact of the new procedure and iterations on the instantaneous pressure distribution is presented in Figure 13. For comparison purpose, we use the same measured acceleration distribution that is used for generating Figure 9, but this time with a virtual boundary and iterations. For this example, the average pressure difference between the initial input and that of the first round of virtual boundary integration is 7.5% of the maximum pressure value, i.e. the initial correction is substantial. Completion of the first iteration with the extended boundaries requires 8 minutes of computation time on a single processor, mid-range speed, Pentium PC. The efficiency of this code will be improved as an on-going effort. After ten iterations, the pressure difference between iteration decreases to 0.07% of the maximum pressure value, i.e. to insignificant levels. As is evident, the pressure distributions in Figure 13 differ significantly from Figure 9 even after one iteration, especially near the forward boundary. The extended virtual boundary greatly reduces the bias in integration path, and the iterations eliminated the dependence on the initial integration along the outer perimeter of the sample area. We believe that the results obtained using the present procedures are very close to the correct answers.

7
Sample pressure measurement results for cavity flow

In the samples presented below, the origin of the coordinates is placed at the leading edge of the cavity. The x and y-axes are pointing downstream and upward, respectively. To illustrate the overall structure of the cavity flow, Figure 14 (a) shows a sample instantaneous velocity distribution and streamlines of the cavity flow. Here the velocity above the cavity is 10m/s and the Reynolds number is 335,000 based on the cavity width. The thickness of the shear layer is around 2mm. Due to the oscillation of the shear layer, the stagnation point of the flow on the downstream wall of the cavity varies significantly from one vector map to the next. In the example shown in Figure
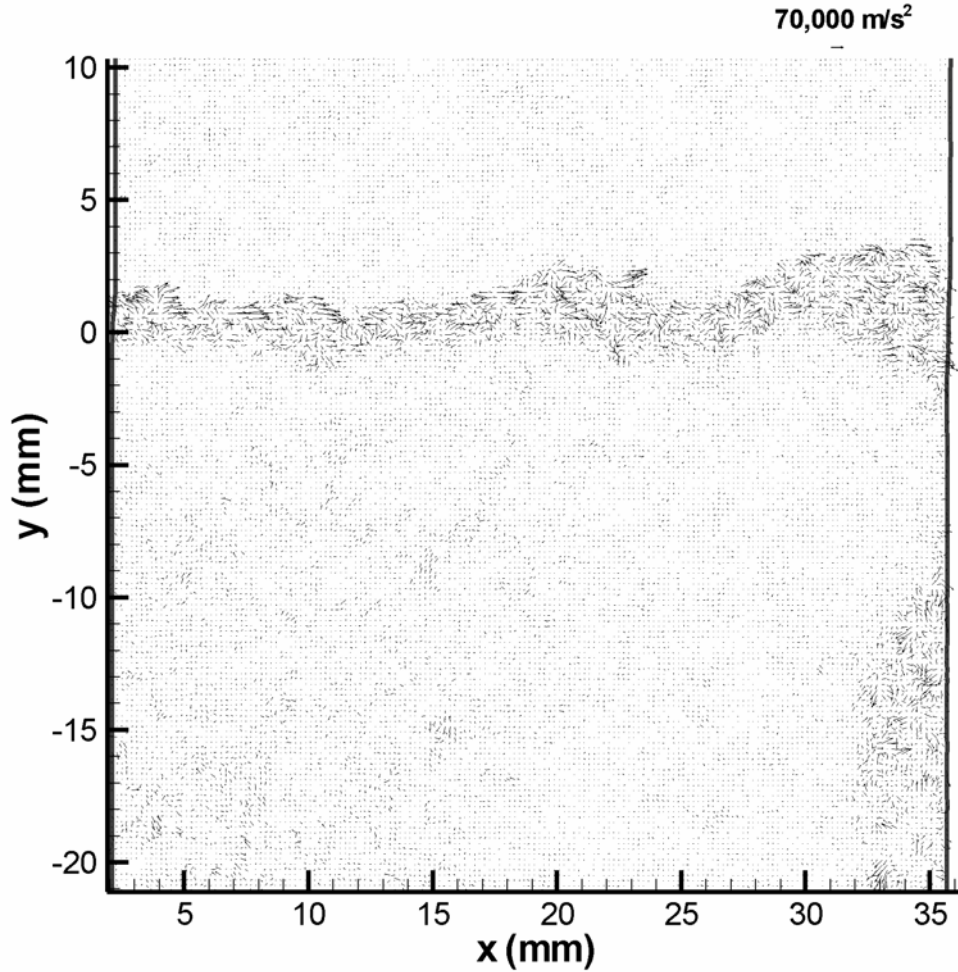
14

Figure 15. Sample instantaneous material acceleration vector map of the cavity flow.

14 (a), the stagnation point is located about 4mm below the trailing corner. The flow field over the cavity may be divided into three regions: (a) Potential flow region; (b) Shear layer, and (c) Recirculation zone, which contains remnants of vorticity swept down from the shear layer. The maximum velocity in the recirculation region is only about 30% of that of the free stream velocity.

To maximize the spatial resolution of the acceleration measurements, we use progressive grid refinement, culminating in 16×16 pixels interrogation window with 50% overlap between windows. The corresponding length scales for a 50.8× 50.8mm field of view are an interrogation window of 0.4×0.4mm, and vector spacing of 0.2 mm. Following the procedures outlined earlier in this paper, we calculate the instantaneous distributions of material acceleration, and then integrate them to obtain the pressure distribution.

A sample instantaneous pressure distribution of the cavity flow is shown in Figure 14 (b), with the corresponding instantaneous material acceleration vector map shown in Figures 15. The local pressure at the upper left corner is selected as the reference level. The streamlines based on a reference frame moving at a speed of half of U_e are overlaid on the pressure contour in order to show the pseudo vortical structure. The maximum magnitude of the material acceleration is around $70,000 m/s^2$, which is on the same order of magnitude as that obtained by La Porta *et al* (2001) for a coaxial counter-rotating disk turbulent flow. The material acceleration vectors appear to congregate as converging/diverging clusters in the shear layer. As expected, comparison of Figures 14(b) and 15 reveals that high pressure develops in regions of flow deceleration, and conversely, pressure minima develop in accelerating regions. These regions are mainly within the shear layer where vorticity are concentrated. However, these pressure maxima /minima apparently have global effects over the entire flow field. The overall picture also varies dramatically due to the oscillation of the shear layer. Clearly, the instantaneous pressure field of the cavity flow is extremely complicated.

15

9
Conclusions and future work

This paper reports the latest development of a non-intrusive measurement technique capable of measuring the instantaneous spatial pressure distribution over a sample area in flow filed. By measuring the distribution of material acceleration with four-exposure PIV, this technique further integrates it to obtain the pressure distribution. With this system, the instantaneous pressure, material acceleration and velocity distributions can be measured simultaneously.

The principles of the procedure are validated using synthetic rotational and stagnation point flows. The standard deviation of the measured instantaneous pressure from the theoretical value is about 1.0%. A key to the success of the application of the technique is to use a local deformation correction method to ensure accurate alignment of the velocity vectors measured by the two CCD cameras. Using this alignment method, the error in terms of the standard deviation of velocity differences due to relative misalignment and distortion is reduced to about 0.01 pixels. To minimize the error of the pressure distribution, an efficient and accurate virtual boundary integration scheme, further enhanced by iteration, is used for the pressure integration. With careful selection of the virtual boundary extension parameter (gap between the virtual and real boundaries) and iteration, the residue error of the converged pressure distribution can be as low as only 0.04% of the dynamic pressure. This technique has been used for the measurements of a cavity shear flow.

In the upcoming series of experiments, the data will be acquired simultaneously with wall pressure measurements. Both instantaneous readings and statistics will be compared. To obtain such pressure statistics, the data analysis procedures needs to be made efficient enough to handle thousands of instantaneous realizations.

10
Acknowledgement

References

Adrian R.J. (1997) Dynamic ranges of velocity and spatial resolution of particle image velocimetry, Meas. Sci. Technol., 8, 1393-1398.

Arndt R.E.A. (2002) Cavitation in vortical flows, Annu. Rev. Fluid Mech. 34, 143-175.

Blake W.K. (1986) Mechanics of flow-induced sound and vibration, Academic Press, Inc.

Brennen C.E. (1995) Cavitation and bubble dynamics, Oxford University Press.

Chen J.; Katz J. (2005) Elimination of peak-locking error in PIV analysis using the correlation mapping method, Meas. Sci. Technol. 16, 1605-1618.

Christensen K.T.; Adrian R.J. (2001) Measurement of instantaneous acceleration fields using particle-image velocimetry, 4th Int. Symp. on PIV, PIV01 Paper 1080.

Christensen K.T. and Adrian R.J. (2002) Measurement of instantaneous Eulerian acceleration fields by particle-image velocimetry: method and accurancy, Exp. Fluids, 33, 759-769.

Chung K.M. (2001) Three-dimensional effect on transonic rectangular cavity flows, Exp. Fluids, 30, 531-536.

Dong P.; Hsu T.Y.; Atsavapranee P.; Wei T. (2001) Digital particle image accelerometry, Exp. Fuids, 30: 626-632.

Girimaji, S.S. (2000) Pressure-strain correlation modelling of complex turbulent flows, J. Fluid Mech., 422, 91-123.

Gopalan S.;Katz J. (2000) Flow structure and modeling issues in the closure region of attached cavitation, Phys. Fluids, 12, 895-911. **Herrmann J.** (1980) Least-squares wave front error of minimum norm, J. Opt. Soc. Am., 70, 28-35.

Gutmark E.; Wygnanski I. (1976) The planar turbulent jet, J. Fluid Mech., 73, 465-495.

Hill R.J.; Thoroddsen S.T. (1997) Experimental evaluation of acceleration correlations for locally isotropic turbulence, Physical Review E, 55, 1600-1606.

Huang H.T.; Fiedler H.E.; Wang J.J. (1993) Limitation and improvement of PIV, Part II: Particle image distortion, a novel technique, Exp. Fluids, 15, 263-273.

Jakobsen M.L.; Dewhirst T.P.; Greated C.A. (1997) Particle image velocimetry for predictions of acceleration fields and force within fluid flows, Meas. Sci. Thechnol., 8, 1502-1516.

La Porta A.; Voth G.A.; Crawford A.M.; Alexander J.; Bodenschatz E. (2001) Fluid particle accelerations in fully developed turbulence, Nature, 409, 1017-1019.

Lin J.C. and Rockwell D. (2001) Organized oscillations of initially turbulent flow past a cavity, AIAA J., 39, 1139-1151.

Liu X. (2001) A study of wake development and structure in constant pressure gradient, Ph.D. dissertation, University of Notre Dame.

Liu, X.; Katz, J. (2003) Measurements of pressure distribution by integrating the material aceleration, Cav03-GS-14-001, Fifth International Symposium on Cavitation (CAV2003), Osaka, Japan, November 1-4, 2003.

Liu X.; Katz J. (2004) Measurements of pressure distribution in a cavity flow by integrating the material aceleration, HT-FED2004-56373, 2004 ASME Heat Transfer/Fluids Engineering Summer Conference, Charlotte, North Carolina, USA, July 11-15, 2004.

Liu X.; Thomas F.O. (2004) Measurement of the turbulent kinetic energy budget of a planar wake flow in pressure gradients, Experiments in Fluids, 37, 469-482.

O'Hern T.J (1990) An experimental investigation of turbulent shear flow cavitation, J. Fluid. Mech. 215, 365–391.

Ooi K. K.; Acosta A. J. (1983) The utilization of specially tailored air bubbles as static pressure sensors in a jet, J. Fluids Engineering, 106, 459-465.

Ott S.; Mann J. (2000) An experimental investigation of the relative diffusion of particle pairs in three-dimensional turbulent flow, J. Fluid Mech., 422, 207-223.

Press W.H.; Teukolsky S.A.; Vetterling W.T.; Flannery B.P. (2002) Numerical recipes in C/C++, the Press Syndicate of the University of Cambridge.

Pope S.B. (2000), Turbulent flows, Cambridge Univ. press.

Ran, B.; Katz, J. (1994) Pressure fluctuations and their effect on cavitation inception within water jets, J. Fluid Mech., 262, 223-263.

Rockwell D.; Knisely C. (1979) The organized nature of flow impingement upon a corner, J. Fluids Mech., 93, 413-432.

Roth G.I. (1998) Developments in particle image velocimetry (PIV) and their application to the measurement of the flow structure and turbulence within a ship bow wave, Ph.D. dissertation, Johns Hopkins University.

Roth G.I.; Katz, J. (2001) Five techniques for increasing the speed and accuracy of PIV interrogation, Meas. Sci. Technol., 12, 238-245.

Southwell W.H. (1980) Wave-front estimation from wave-front slope measurements, J. Opt. Soc. Am., 70, 998-1006.

Sridhar G. and Katz J. (1995) Drag and lift forces on microscopic bubbles entrained by a vortex, Phys. Fluids, 7, 389-399.

Tang Y.P.; Rockwell D. (1983) Instantaneous pressure fields at a corner associated with vortex impingement, J. Fluid Mech., 126, 187-204.

Thomas F.O.; Liu X. (2004) An experimental investigation of symmetric and asymmetric turbulent wake development in pressure gradient, Physics of Fluids, Vol. 16, No.5, pp1725-1745.

Vedula P.; Yeung P.K. (1999) Similarity scaling of acceleration and pressure statistics in numerical simulations of isotropic turbulence, Phys. Fluids, 11, 1208-1220.

Voth G.A.; Satyanarayan K.; Bodenschatz E. (1998) Lagrangian acceleration measurements at large Reynolds numbers, Phys. Fluids, 10, 2268-2280.

Wygnanski, I.; Fiedler, H. (1969) Some measurements in the self-preserving jet, J. Fluid Mech., 38, 577-612.

Yeung P.K. (2001) Lagrangian characteristics of turbulence and scalar transport in direct numerical simulations, J. Fluid Mech., 427, 241-274.

Yeung P.K. (2002) Lagrangian investigations of turbulence, Annu. Rev. Fluid Mech., 34, 115-142.